JOURNAL OF SYNCHROTRON RADIATION

ISSN 1600-5775

Received 11 January 2018
Accepted 17 May 2018

Edited by A. Momose, Tohoku University, Japan

Keywords: X-ray imaging; phase contrast; analyzer-based imaging; information retrieval; USAXS; rocking curves; three-image algorithms.

Absorption, refraction and scattering retrieval in X-ray analyzer-based imaging

Zhili Wang,[a,b]* Dalin Liu,[a] Jin Zhang,[c] Wanxia Huang,[c] Qingxi Yuan,[c]* Kun Gao[d] and Zhao Wu[d]

[a]School of Electronics and Applied Physics, Hefei University of Technology, Hefei, Anhui 230009, People's Republic of China, [b]Beijing Advanced Innovation Center for Imaging Technology, Capital Normal University, Beijing 100048, People's Republic of China, [c]Institute of High Energy Physics, Chinese Academy of Science, Beijing 100049, People's Republic of China, and [d]National Synchrotron Radiation Laboratory, University of Science and Technology of China, Anhui 230026, People's Republic of China. *Correspondence e-mail: dywangzl@hfut.edu.cn, yuanqx@ihep.ac.cn

A three-image algorithm is proposed in order to retrieve the absorption, refraction and ultra-small-angle X-ray scattering (USAXS) properties of the object in X-ray analyzer-based imaging. Based on the Gaussian fitting to the rocking curve, the novel algorithm is theoretically derived and presented, and validated by synchrotron radiation experiments. Compared with multiple-image radiography, this algorithm only requires a minimum of three intensity measurements, and is therefore advantageous in terms of simplified acquisition procedure and reduced data collection times, which are especially important for specific applications such as *in vivo* imaging and phase tomography. Moreover, the retrieval algorithm can be specialized to particular cases where some degree of *a priori* knowledge on the object is available, potentially reducing the minimum number of intensity measurements to two. Furthermore, the effect of angular mis-alignment on the accuracy of the retrieved images was theoretically investigated, which can be of use in image interpretation and optimization of the data acquisition procedure.

1. Introduction

Over the last decades, X-ray analyzer-based imaging (ABI) as a phase-contrast imaging technique has attracted much attention in the scientific community. Unlike conventional absorption-based imaging, ABI also derives contrast from the phase modulations induced by the object onto the transmitted X-ray beam. These two effects can be described in terms of the complex refractive index $n = 1 - \delta + i\beta$. While the real part δ corresponds to the phase shift, the imaginary part β is responsible for the absorption. Since δ is much greater than β in the hard X-ray regime (Momose & Fukuda, 1995), ABI is in principle capable of providing improved contrast compared with absorption-based imaging, especially for weakly attenuating samples, such as biomedical tissues (Davis *et al.*, 1995; Bravin *et al.*, 2013). Besides absorption and refraction (based on the derivative of the X-ray phase shift induced by the object), ultra-small-angle X-ray scattering (USAXS) also has an important contribution to the generation of the image contrast (Pfeiffer *et al.*, 2008). This effect is characterized by angles on the micro-radian scale, partially falls within the acceptance of the analyzer crystal and plays the role of broadening the observed rocking curve (RC).

In X-ray ABI, the contrast in the acquired sample projections is given by a mixture of absorption, refraction and USAXS information. This information superposition can make the image interpretation ambiguous in some cases. In

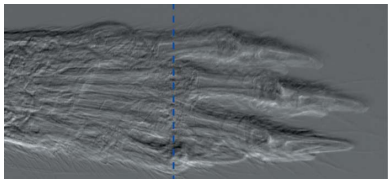

order to separate three different physical effects and accurately quantify them, three distinct approaches have been developed. In the first approach, leading terms of the Taylor expansion of the RC at the working points are used to describe the intensity changes (Chapman *et al.*, 1997; Rigon *et al.*, 2003, 2007*a*,*b*; Chou *et al.*, 2007). Phantom studies showed that these algorithms produced reliable results when the refraction angle and the width of USAXS were small compared with the full width at half-maximum (FWHM) of the RC, and when the coefficients of the Taylor expansion remained constant within sufficient ranges around the working points (Rigon *et al.*, 2007*a*,*b*; Chou *et al.*, 2007). The second approach is to fit a functional form to the measured RCs. A Gaussian curve fitting (GCF) algorithm was proposed by Nesterets *et al.* (2006) and used in image analysis (Diemoz *et al.*, 2012). Although the GCF algorithm can provide accurate estimates of the different quantities, an obvious drawback of the GCF algorithm is its excessive computation times in locally fitting the function pixel by pixel. Similar algorithms have also been proposed based on the use of other fitting functions: Voigtian (Suhonen *et al.*, 2007), Pearson VII (Majidi *et al.*, 2014) and Cosine (Bao *et al.*, 2015). The third approach is called multiple-image radiography (MIR), where the RC is parameterized from multiple images acquired at several different angular positions of the analyzer crystal without curve fitting. The sample RC (measured with the sample) was then compared with the reference RC (without the sample) pixel by pixel. The differences between the RCs allowed full separation of the absorption, refraction and USAXS signals (Oltulu *et al.*, 2003; Wernick *et al.*, 2003; Brankov *et al.*, 2006). Alternatively, absorption, refraction and USAXS images can be calculated from the differences in the zeroth-, first- and second-moments of the RCs (Pagot *et al.*, 2003). Although this approach is in principle very stable with respect to noise, an important limitation is its increased acquisition time and dose deposition to the sample since many measurements need to be performed. Therefore, there remains an important need to develop efficient data acquisition strategies and phase retrieval algorithms for ABI.

In this work, we propose a three-image algorithm to retrieve the absorption, refraction and USAXS properties of the sample. First, we present the ABI image formation model based on the Gaussian fitting to the RC and radiative transfer theory (Khelashvili *et al.*, 2006), followed by the derivation of analytical formulae for information retrieval. It is shown that a minimum of three intensity measurements are sufficient to separate the absorption, refraction and USAXS images. Furthermore, the exploitation of *a priori* knowledge that might be available about the sample can reduce the minimum number of intensity measurements to two. Finally, the proposed algorithm is validated by synchrotron radiation experiments, and the retrieved results are compared with those obtained by MIR and discussed.

2. Three-image algorithm for information retrieval

The typical ABI setup is schematically shown in Fig. 1(*a*). A first crystal is used to create a parallel, monochromatic X-ray beam from the incoming radiation, and a second analyzer crystal, placed between the sample and the detector, acts as an angular filter of the beam transmitted through the sample. Both the monochromator and analyzer crystals are used in the reflection geometry. Before being detected, the X-ray beam is modulated by the RC of the analyzer crystal, which represents the detected intensity as a function of the angular position θ of the analyzer crystal in the absence of the sample. Typically, the RC of the analyzer crystal has a FWHM, *i.e.* the Darwin width $\theta_{\rm D}$, of the order of a few microradians.

When a sample is placed between the monochromator and analyzer crystals, the X-ray beam will be locally attenuated, refracted and scattered. It has been well established that the measured intensity $I(\theta; x, y)$ can be expressed as the following convolution (Wernick *et al.*, 2003; Majidi *et al.*, 2014),

$$I(\theta; x, y) = I_0 R_{\rm int}(\theta) \otimes f(\theta; x, y) \qquad (1)$$

where I_0 is the incident photon number per pixel, $R_{\rm int}(\theta)$ is the intrinsic RC, $f(\theta; x, y)$ is the sample's angular response function, and $\otimes$ denotes one-dimensional convolution. Strictly speaking, the intrinsic RC can be quite complicated without analytical expressions. Fortunately, $R_{\rm int}(\theta)$ can be approximately fitted by using appropriate functions (Nesterets *et al.*, 2006; Chou *et al.*, 2007; Suhonen *et al.*, 2007; Majidi *et al.*, 2014; Bao *et al.*, 2015), which facilitates the development of information retrieval algorithms and further image interpretation. Here we adopt a Gaussian function to fit the intrinsic RC. Note that this approximation has been explicitly or implicitly used for information extraction (Suortti *et al.*, 2013) and image

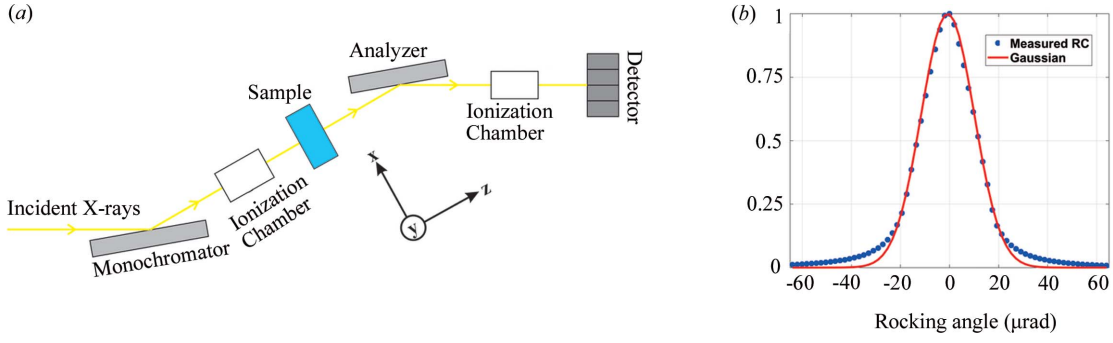

Figure 1
(*a*) Schematic diagram of the ABI setup. (*b*) Measured (dotted line) and Gaussian fitted (solid line) intrinsic RC using 15 keV X-rays.

analysis (Diemoz *et al.*, 2010). Under this approximation, the normalized intrinsic RC can be written as

$$R_{\rm int}(\theta) = \exp\left(-\frac{\theta^2}{2\sigma_\theta^2}\right), \tag{2}$$

where σ_θ is the standard deviation, and satisfies $\sigma_\theta = \theta_{\rm D}/[2(\ln 4)^{1/2}]$.

Consider the sample's angular response function $f(\theta; x, y)$, the full expression of which was derived using radiative transfer theory and uniquely described by eight object parameters (Khelashvili *et al.*, 2006). Here, we adopt the approximately simplified expression of the sample's angular response function given by (Chou *et al.*, 2007; Majidi *et al.*, 2014)

$$f(\theta; x, y) = \frac{I_R(x, y)}{[2\pi\sigma_s^2(x, y)]^{1/2}} \exp\left\{-\frac{[\theta - \Delta\theta(x, y)]^2}{2\sigma_s^2(x, y)}\right\}, \tag{3}$$

where $I_R(x, y)$ represents the sample's apparent absorption, $\sigma_s^2(x, y)$ is the variance of the USAXS distribution, and $\Delta\theta(x, y) = -\int \left[\partial\delta(x, y, z)/\partial x\right] {\rm d}z$ is the X-ray's refraction induced by the sample. From measurements of the three parameters of the angular response function, we can obtain absorption, refraction and USAXS signals, which can be displayed in the form of images.

On substitution of equations (2) and (3) into equation (1), we can yield the following expression for the measured intensity,

$$\begin{aligned} I(\theta; x, y) &= I_0 R_{\rm int}(\theta) \otimes f(\theta; x, y) \\ &= I_0 \sigma_\theta \frac{I_R(x, y)}{\sigma(x, y)} \exp\left\{-\frac{[\theta - \Delta\theta(x, y)]^2}{2\sigma^2(x, y)}\right\}, \end{aligned} \tag{4}$$

with $\sigma^2 = \sigma_\theta^2 + \sigma_s^2$. Equation (4) presents the image formation model of ABI on a pixel-by-pixel basis, and will be used for the derivation of a three-image algorithm for information retrieval.

To fully separate the sample's absorption, refraction and USAXS images, let us consider three intensity measurements acquired with the angular position of the analyzer crystal set to $\theta_1 = -\theta_3$ and $\theta_2 = 0$. By use of equation (4), the following system can be written:

$$I_k(x, y) = I_0 \sigma_\theta \frac{I_R(x, y)}{\sigma(x, y)} \exp\left\{-\frac{[\theta_k - \Delta\theta(x, y)]^2}{2\sigma^2(x, y)}\right\}, \tag{5}$$

for $k = 1, 2, 3$. As derived in Appendix *A*, equation (5) can be analytically solved to give the absorption image $I_R(x, y)$, the refraction image $\Delta\theta(x, y)$ and the USAXS image $\sigma_s^2(x, y)$,

$$\begin{cases} I_R(x, y) = \dfrac{I_2\theta_1}{I_0\sigma_\theta} \dfrac{1}{(C_1 + C_2)^{1/2}} \exp\left[\dfrac{1}{8}\dfrac{(C_1 - C_2)^2}{C_1 + C_2}\right], \\ \Delta\theta(x, y) = \dfrac{\theta_1}{2}\dfrac{C_2 - C_1}{C_1 + C_2}, \\ \sigma_s^2(x, y) = \dfrac{\theta_1^2}{C_1 + C_2} - \sigma_\theta^2, \end{cases} \tag{6}$$

where $C_1 = \ln\left(I_2/I_1\right)$ and $C_2 = \ln\left(I_2/I_3\right)$. Equation (6) allows us to separate the contributions to I_1, I_2 and I_3 coming from absorption, refraction and USAXS properties of the sample.

Moreover, these solutions can be further specialized when *a priori* information about the sample is available. For samples with negligible refraction, *i.e.* $\Delta\theta = 0$, the absorption and USAXS images can be retrieved by using only two intensity measurements,

$$\begin{cases} I_R(x, y) = \dfrac{I_2}{I_0\sigma_\theta} \dfrac{\theta_1}{(2C)^{1/2}}, \\ \sigma_s^2(x, y) = \dfrac{\theta_1^2}{2C} - \sigma_\theta^2(x, y), \end{cases} \tag{7}$$

with $C = -\ln\left(I_1/I_2\right)$. Similarly, in the case of negligible scattering, *i.e.* $\sigma_s = 0$, one can retrieve the absorption and refraction images from two intensity measurements I_1 and I_3 by

$$\begin{cases} I_R(x, y) = \dfrac{I_1}{I_0} \exp\left[\dfrac{\left(\theta_1^2 - \sigma_\theta^2 D\right)^2}{2\theta_1^2\sigma_\theta^2}\right], \\ \Delta\theta(x, y) = \dfrac{\sigma_\theta^2}{\theta_1} D, \end{cases} \tag{8}$$

where $D = \ln\left(I_1/I_3\right)^{1/2}$.

A distinct feature of the proposed algorithm is that it requires only three intensity measurements to be acquired at different angular positions of the analyzer crystal. Compared with the three-image DEI (Rigon *et al.*, 2007*a*,*b*), the advantage is that no Taylor expansion of the RC is used, and therefore the accuracy of retrieval results will not be compromised when the refraction signal and/or the width of USAXS are comparable with the FWHM of the RC. In comparison with the GCF algorithm, the computation time is much shorter, since no Gaussian fitting procedure has to be repeated pixel by pixel. Comparing with multiple-image radiography, the proposed algorithm only requires three intensity measurements as input, and therefore is advantageous in terms of reduced acquisition time and dose deposition to the sample. This can be important in applications such as *in vivo* studies (Coan *et al.*, 2010) and clinical studies (Suortti *et al.*, 2013). The dynamic range of the three-image algorithm, however, may be limited within the RC, while the dynamic range of MIR can be greater than the FWHM of the RC. Detailed analysis on this topic will appear in our future work.

3. Experimental validation

The novelty of the proposed three-image algorithm lies in its ability to enable the simultaneous absorption, refraction and scattering retrieval by use of only three intensity measurements. In order to test its validity, synchrotron radiation experiments were performed.

Experimental imaging studies were conducted at the 4W1A beamline of Beijing Synchrotron Radiation Facility (Yuan

et al., 2006, 2012). A schematic of the experimental setup is shown in Fig. 1(*a*). A first Si (111) crystal acted as the beam monochromator, and X-rays with a photon energy of 15 keV were selected. A second Si (111) crystal was used to analyze the beam exiting from the sample. The intensity was recorded by use of a high-resolution X-ray digital camera system FDS694 by Photonic Science Ltd with a pixel size of 4.5 µm.

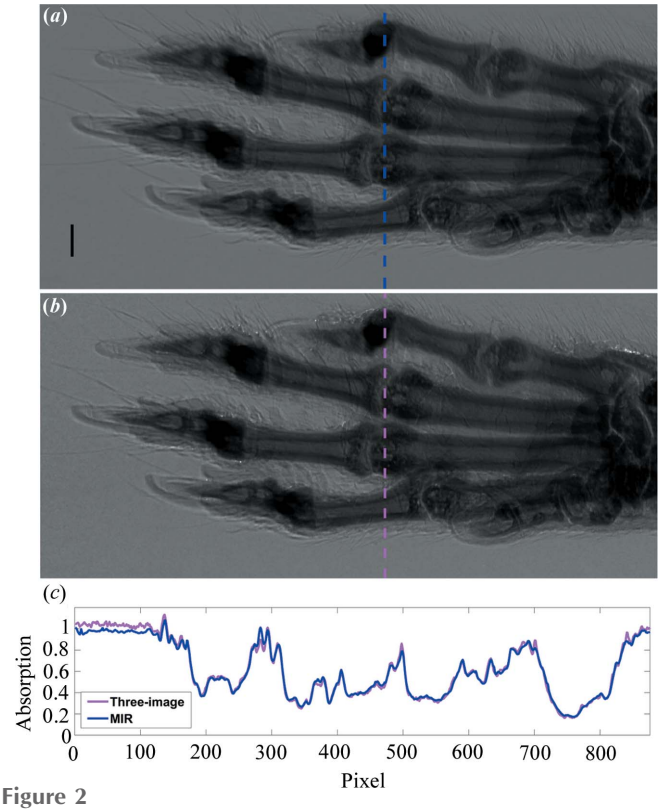

Figure 2
(*a*) Absorption image obtained with MIR; (*b*) absorption image obtained with the three-image algorithm; (*c*) line profiles along the dashed line. Scale bar = 0.45 mm.

For the MIR algorithm (Wernick *et al.*, 2003), the intensity measurements were acquired at 85 analyzer positions, ranging from −84 to 84 µrad with 2 µrad increments. At each analyzer position, a flat-field image without the sample was acquired, which resulted in measurement of the intrinsic RC $R_{\rm int}(\theta)$. Dark-field images were also obtained and utilized for correction of experimental data. As illustrated in Fig. 1(*b*), the Gaussian fitting was quantitatively in good agreement with the measured intrinsic RC, supported by the fact that the calculated correlation coefficient has a value greater than 0.99. The images produced by MIR served as ground truth images and were used for a quantitative comparison with those obtained by the proposed algorithm. For the novel three-image algorithm, three intensity measurements corresponding to $\theta_1 = -21.3$ µrad, $\theta_2 = 0$ µrad and $\theta_3 = 23.3$ µrad were used to retrieve the absorption, refraction and USAXS images [equation (6)]. The obtained results were then compared with those correspondingly obtained with MIR.

Fig. 2 shows the absorption images of a demineralized mouse joint. An excellent agreement can be clearly found in the absorption maps obtained with the two algorithms, shown in Figs. 2(*a*) and 2(*b*), respectively. Furthermore, Fig. 2(*c*) shows the line profiles of the absorption images at the position indicated by the dotted line. The agreement of the two line profiles is quantitatively excellent, confirmed by the value of the calculated correlation coefficient $R = 0.995$.

The retrieved refraction images of a demineralized mouse joint are shown in Fig. 3. Figs. 3(*a*) and 3(*b*) show the refraction maps retrieved by MIR and the novel three-image algorithm, respectively. As can be seen, these two images are qualitatively quite similar. For a quantitative evaluation, the diagram in Fig. 3(*c*) shows the line profiles along the rows marked by the dashed line. The blue solid line corresponds to the MIR approach while the magenta line is obtained using the novel three-image algorithm. As expected, the two line profiles show a quantitatively good agreement between the

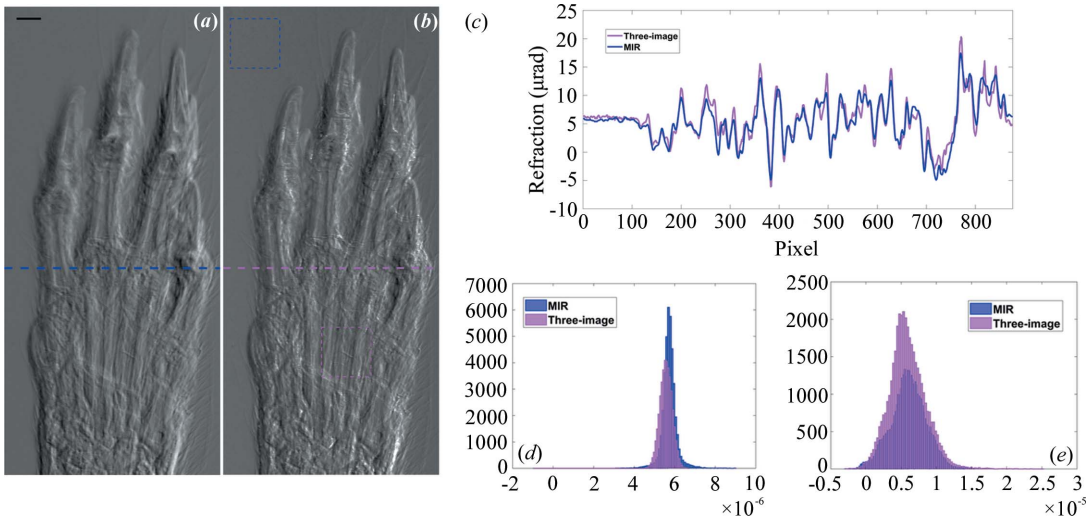

Figure 3
(*a*) Retrieved refraction image by MIR; (*b*) retrieved refraction image by the three-image algorithm; (*c*) line profiles along the dashed line; (*d*) histogram of the retrieved refraction signal in the background region; (*e*) histogram of the retrieved refraction signal in a region within the sample. Scale bar = 0.45 mm.

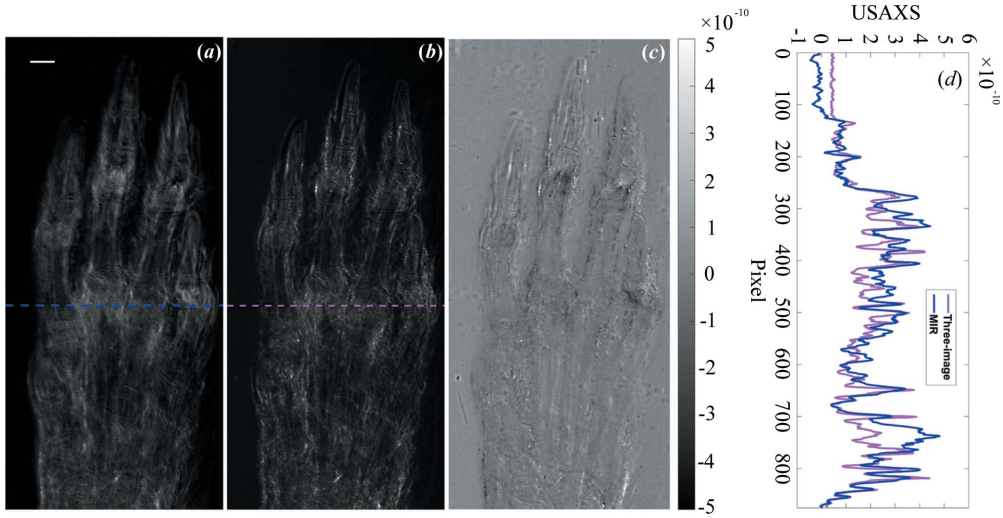

Figure 4
(*a*) USAXS image produced by MIR; (*b*) USAXS image by the three-image algorithm; (*c*) difference obtained from the previous images; (*d*) line profiles along the dashed line. Scale bar = 0.45 mm.

three-image and MIR algorithms, with a calculated correlation coefficient $R = 0.94$. Some minor differences are also noticeable between the two line profiles. This can be understood by considering that firstly only three intensity measurements are used by the novel three-image algorithm for information retrieval, and secondly the two intensity measurements I_1 and I_3 are acquired at angular positions where the intrinsic RC only has a value of 0.15. Another quantification of the similarity of the two results is visually appreciable from Figs. 3(*d*) and 3(*e*) showing the histograms taken in a region within the sample and the background, respectively, marked by the rectangles. Both distributions obtained with the novel algorithm are consistently wider, indicating a larger dynamics and larger fluctuations. It is of great importance to reiterate that the differences are actually minor and the retrieved results obtained with the two algorithms are largely consistent.

The USAXS images, obtained from the same experimental data set, are shown in Fig. 4. As illustrated in Figs. 4(*a*) and 4(*b*), a qualitative comparison of the images clearly shows that the result of the three-image algorithm is compatible with that of MIR. To test the accuracy of our algorithm, the difference between the two independent maps in Figs. 4(*b*) and 4(*a*), respectively, is presented in Fig. 4(*c*). The result indicates a substantial equivalence of the two retrieved images, with the novel algorithm rendering a wider distribution in the background region and less absorbing part of the sample. On the other hand, the MIR algorithm yields a wider distribution in the central regions where the sample is highly absorbing. In addition, Fig. 4(*d*) shows the line profiles taken along the dashed line of the USAXS images for a quantitative comparison. Despite the small local differences, the results obtained with both algorithms are consistent, thus confirming the feasibility of the proposed algorithm.

Furthermore, it is also possible to retrieve the absorption and refraction images by use of only two intensity measurements. To test this possibility, images of a plastic rod, which produced negligible scattering, were post-processed using equation (8). Results are displayed in Figs. 5(*a*) and 5(*b*) for the refraction images obtained by MIR and the three-image

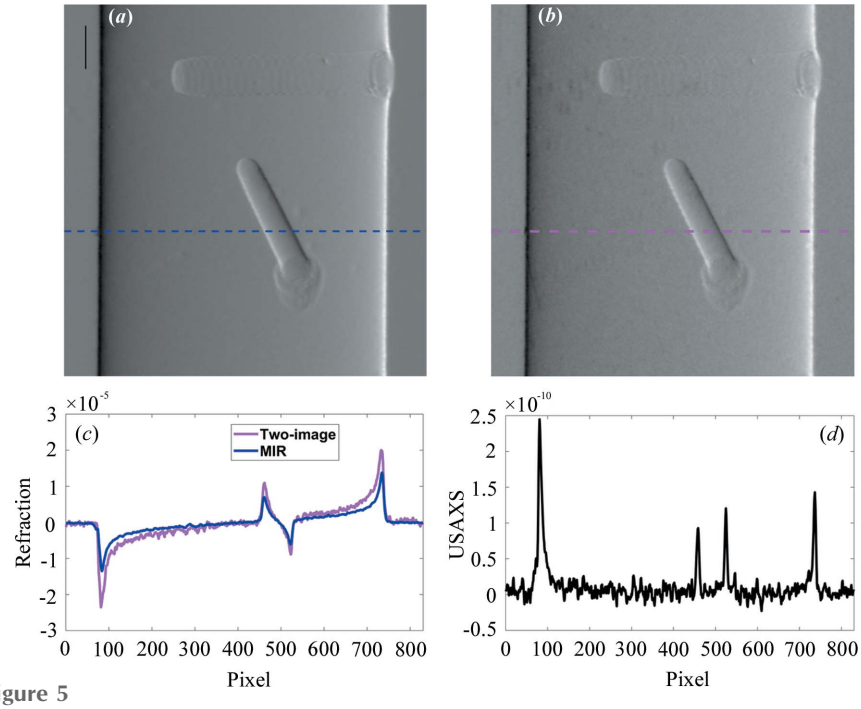

Figure 5
Refraction image of a plastic rod obtained by MIR (*a*) and by the three-image algorithm (*b*). (*c*) Line profiles along the dashed line; (*d*) USAXS image obtained by MIR. Scale bar = 0.45 mm.

algorithm, respectively. Note that the refraction images obtained with only two intensity measurements are comparable with that obtained by the MIR algorithm taking into account the higher statistics of the latter. On the other hand, some discrepencies can also be observed, especially at the edges of the rod. This can be explained by the fact that the very large refraction in these regions leads to the violation of the geometrical optics approximation (Nesterets *et al.*, 2006; Diemoz *et al.*, 2010). This violation results in strong USAXS signals at the edges of the rod, as shown in Fig. 5(*d*). This considerably increases the range of refracted X-rays in the three-image algorithm.

4. Discussion

As shown in equation (5), the presented three-image requires that the two intensity measurements I_1 and I_3 are acquired at $\theta_1 = -\theta_3$. While it is relatively not so difficult to acquire the peak intensity I_2, it is difficult in experiments to precisely set the analyzer crystal at prescribed angular positions. Therefore, it is quite essential to investigate how the angular mis-alignment affects the accuracy of the retrieved results. Consider the three intensity measurements acquired at $\theta_1 = \theta_0$, $\theta_2 = 0$ and $\theta_3 = -\theta_0 + \varepsilon_\theta$, with ε_θ being the angular mis-alignment. By use of equations (5) and (6), we can yield the following retrieval results,

$$\begin{cases} I_R' = \dfrac{I_R\theta_0}{[\theta_0^2 - \varepsilon_\theta(\theta_0 - \Delta\theta)]^{1/2}} \exp\left\{\dfrac{\varepsilon_\theta \Delta\theta}{2\sigma^2}\left[\left(\dfrac{\Delta\theta}{\theta_0}\right)^2 - 1\right]\right\}, \\ \Delta\theta' = \Delta\theta + \dfrac{\varepsilon_\theta}{2}\left[2\left(\dfrac{\Delta\theta}{\theta_0}\right)^2 + \dfrac{\Delta\theta}{\theta_0} - 1\right], \\ (\sigma_s^2)' \simeq \sigma_s^2 + \dfrac{\varepsilon_\theta \sigma^2}{\theta_0}\left(1 - \dfrac{\Delta\theta}{\theta_0}\right), \end{cases} \tag{9}$$

whose detailed deviation is given in Appendix *B*. As shown in equation (9), the inaccuracy in the absorption image, defined as $I_R'/I_R - 1$, depends on the angular mis-alignment ε_θ in a quite complicated form. Besides, it is also dependent on the sample's refraction and USAXS signals, and has no dependence on the absorption signal. On the other hand, for the refraction image, the inaccuracy, defined as $\Delta\theta' - \Delta\theta$, is linearly proportional to the angular mis-alignment ε_θ, and is only dependent on the ratio $\Delta\theta/\theta_0$, and independent of the sample's absorption and USAXS signals. Finally, the inaccuracy in the USAXS image, defined as $(\sigma_s^2)' - \sigma_s^2$, varies linearly as a function of the quantities $\varepsilon_\theta/\theta_0$ and $\Delta\theta/\theta_0$. It is also dependent on the USAXS signal linearly through σ^2 and independent of the sample's absorption signal.

5. Conclusion

A three-image algorithm has been proposed for absorption, refraction and scattering retrieval in X-ray analyzer-based imaging. Based on the Gaussian fitting to the intrinsic RC, the information retrieval algorithm is theoretically derived and presented, and validated by results from synchrotron radiation experiments. The retrieved results are quantitatively comparable with those obtained with multiple-image radiography. A minimum of three intensity measurements acquired at different angular positions are required in order to separate the absorption, refraction and USAXS properties of the sample. Compared with MIR, this three-image algorithm is advantageous in terms of reduced exposure time and radiation dose delivered to the sample. Therefore, we can expect widespread application of the novel method in areas where exposure time and/or radiation dose are critical. Moreover, it is shown that the algorithm can also be adapted for particular cases in which some *a priori* information about the sample is available, limiting the number of required intensity measurements to two. Finally, the effect of angular mis-alignment on the accuracy of the three retrieved images is theoretically investigated. The results are useful for image interpretation and optimization of data acquisition procedure.

APPENDIX *A*
Detailed derivation of equation (6)

According to equation (4), the three intensity measurements are given by

$$\begin{cases} I_1 = \dfrac{I_0\sigma_\theta}{\sigma} I_R \exp\left[-\dfrac{(\theta_1 - \Delta\theta)^2}{2\sigma^2}\right], \\ I_2 = \dfrac{I_0\sigma_\theta}{\sigma} I_R \exp\left[-\dfrac{(0 - \Delta\theta)^2}{2\sigma^2}\right], \\ I_3 = \dfrac{I_0\sigma_\theta}{\sigma} I_R \exp\left[-\dfrac{(\theta_1 + \Delta\theta)^2}{2\sigma^2}\right]. \end{cases} \tag{10}$$

Based on equation (10),

$$\begin{cases} C_1 = -\ln\left(\dfrac{I_1}{I_2}\right) = \left[\dfrac{(\theta_1 - \Delta\theta)^2}{2\sigma^2}\right] - \left[\dfrac{(0 - \Delta\theta)^2}{2\sigma^2}\right] = \dfrac{\theta_1^2 - 2\theta_1\Delta\theta}{2\sigma^2}, \\ C_2 = -\ln\left(\dfrac{I_3}{I_2}\right) = \left[\dfrac{(\theta_1 + \Delta\theta)^2}{2\sigma^2}\right] - \left[\dfrac{(0 - \Delta\theta)^2}{2\sigma^2}\right] = \dfrac{\theta_1^2 + 2\theta_1\Delta\theta}{2\sigma^2}. \end{cases} \tag{11}$$

A1.1. The refraction $\Delta\theta$. By use of equation (11), one can yield

$$\frac{C_2 - C_1}{C_2 + C_1} = \frac{2\Delta\theta}{\theta_1}, \tag{12}$$

and then the refraction $\Delta\theta$ can be retrieved by

$$\Delta\theta = \frac{\theta_1}{2}\frac{C_2 - C_1}{C_2 + C_1}. \tag{13}$$

A1.2. The USAXS σ_s^2. On substitution of equation (13) into equation (11), one can obtain

$$\sigma^2 = \frac{\theta_1^2 - 2\theta_1\Delta\theta}{2C_1} = \frac{\theta_1^2}{2C_1}\left(1 - \frac{C_2 - C_1}{C_2 + C_1}\right) = \frac{\theta_1^2}{C_1 + C_2}, \tag{14}$$

which then leads to

$$\sigma_s^2 = \frac{\theta_1^2}{C_1 + C_2} - \sigma_\theta^2. \tag{15}$$

A1.3. The absorption I_R. Substituting equations (13) and (14) into equation (10), one can retrieve the absorption I_R,

$$\begin{aligned} I_R &= \frac{I_2\sigma}{I_0\sigma_\theta}\exp\left[\frac{(0-\Delta\theta)^2}{2\sigma^2}\right] \\ &= \frac{I_2\theta_1}{I_0\sigma_\theta}\frac{1}{(C_1+C_2)^{1/2}}\exp\left[\frac{1}{8}\frac{(C_1-C_2)^2}{C_1+C_2}\right]. \end{aligned} \tag{16}$$

APPENDIX *B*
Detailed derivation of equation (9)

By use of equation (4), the three acquired intensity measurements are given by,

$$\begin{cases} I_1 = \dfrac{I_0\sigma_\theta}{\sigma} I_R \exp\left[-\dfrac{(\theta_0-\Delta\theta)^2}{2\sigma^2}\right], \\ I_2 = \dfrac{I_0\sigma_\theta}{\sigma} I_R \exp\left[-\dfrac{(0-\Delta\theta)^2}{2\sigma^2}\right], \\ I_3 = \dfrac{I_0\sigma_\theta}{\sigma} I_R \exp\left[-\dfrac{\left(-\theta_0+\varepsilon_\theta-\Delta\theta\right)^2}{2\sigma^2}\right]. \end{cases} \tag{17}$$

On substitution of equation (17) into equation (13), one can retrieve the refraction by,

$$\begin{aligned} \Delta\theta' &= \frac{2\theta_0^2\Delta\theta - \varepsilon_\theta\theta_0(\theta_0+\Delta\theta)}{2\theta_0^2 - 2\varepsilon_\theta(\theta_0+\Delta\theta)} \\ &= \Delta\theta + \frac{2\varepsilon_\theta\Delta\theta(\theta_0+\Delta\theta) - \varepsilon_\theta\theta_0(\theta_0+\Delta\theta)}{2\theta_0^2 - 2\varepsilon_\theta(\theta_0+\Delta\theta)} \\ &\simeq \Delta\theta + \frac{\varepsilon_\theta}{2}\left[2\left(\frac{\Delta\theta}{\theta_0}\right)^2 + \frac{\Delta\theta}{\theta_0} - 1\right], \end{aligned} \tag{18}$$

and the USAXS by

$$\begin{aligned} \left(\sigma_s^2\right)' &= \sigma^2\frac{\theta_0^2}{\theta_0^2 - \varepsilon_\theta(\theta_0+\Delta\theta)} - \sigma_\theta^2 \\ &= \sigma^2 - \sigma_\theta^2 + \frac{\varepsilon_\theta\sigma^2(\theta_0+\Delta\theta)}{\theta_0^2 - \varepsilon_\theta(\theta_0+\Delta\theta)} \\ &\simeq \sigma_s^2 + \frac{\varepsilon_\theta\sigma^2}{\theta_0}\left(1 - \frac{\Delta\theta}{\theta_0}\right), \end{aligned} \tag{19}$$

and the absorption by

$$\begin{aligned} I_R' &= \frac{I_R\theta_0}{\sigma}\exp\left[-\frac{(0-\Delta\theta)^2}{2\sigma^2}\right]\frac{1}{(C_1+C_2)^{1/2}} \\ &\quad\times\exp\left[\frac{1}{8}\frac{(C_1-C_2)^2}{C_1+C_2}\right] \\ &= \frac{I_R\theta_0}{[\theta_0^2 - \varepsilon_\theta(\theta_0-\Delta\theta)]^{1/2}}\exp\left[\frac{\varepsilon_\theta\Delta\theta}{2\sigma^2}\frac{\Delta\theta^2-\theta_0^2}{\theta_0^2 - \varepsilon_\theta(\theta_0+\Delta\theta)}\right] \\ &\simeq \frac{I_R\theta_0}{[\theta_0^2 - \varepsilon_\theta\theta_0 - \Delta\theta)]^{1/2}}\exp\left\{\frac{\varepsilon_\theta\Delta\theta}{2\sigma^2}\left[\left(\frac{\Delta\theta}{\theta_0}\right)^2 - 1\right]\right\}. \end{aligned} \tag{20}$$

Funding information

This work was supported by National Natural Science Foundation of China (grant No. U1532113; grant No. 11475170; award No. 61671311; grant No. 11505188; grant No. 11205157).

References

Bao, Y., Wang, Y., Li, P., Wu, Z., Shao, Q., Gao, K., Wang, Z., Ju, Z., Zhang, K., Yuan, Q., Huang, W., Zhu, P. & Wu, Z. (2015). *J. Synchrotron Rad.* **22**, 786–795.

Brankov, J. G., Wernick, M. N., Yang, Y., Li, J., Muehleman, C., Zhong, Z. & Anastasio, M. A. (2006). *Med. Phys.* **33**, 278–289.

Bravin, A., Coan, P. & Suortti, P. (2013). *Phys. Med. Biol.* **58**, R1–35.

Chapman, D., Thomlinson, W., Johnston, R., Washburn, D., Pisano, E., Gmür, N., Zhong, Z., Menk, R., Arfelli, F. & Sayers, D. (1997). *Phys. Med. Biol.* **42**, 2015–2025.

Chou, C. Y., Anastasio, M. A., Brankov, J. G., Wernick, M. N., Brey, E. M., Connor, D. M. Jr & Zhong, Z. (2007). *Phys. Med. Biol.* **52**, 1923–1945.

Coan, P., Wagner, A., Bravin, A., Diemoz, P. C., Keyriläinen, J. & Mollenhauer, J. (2010). *Phys. Med. Biol.* **55**, 7649–7662.

Davis, T. J., Gao, D., Gureyev, T. E., Stevenson, A. W. & Wilkins, S. W. (1995). *Nature (London)*, **373**, 595–598.

Diemoz, P. C., Bravin, A., Langer, M. & Coan, P. (2012). *Opt. Express*, **20**, 27670–27690.

Diemoz, P. C., Coan, P., Glaser, C. & Bravin, A. (2010). *Opt. Express*, **18**, 3494–3509.

Khelashvili, G., Brankov, J. G., Chapman, D., Anastasio, M. A., Yang, Y., Zhong, Z. & Wernick, M. N. (2006). *Phys. Med. Biol.* **51**, 221–236.

Majidi, K., Li, J., Muehleman, C. & Brankov, J. G. (2014). *Phys. Med. Biol.* **59**, 1877–1897.

Momose, A. & Fukuda, J. (1995). *Med. Phys.* **22**, 375–379.

Nesterets, Ya. I., Coan, P., Gureyev, T. E., Bravin, A., Cloetens, P. & Wilkins, S. W. (2006). *Acta Cryst.* A**62**, 296–308.

Oltulu, O., Zhong, Z., Hasnah, M., Wernick, M. N. & Chapman, D. (2003). *J. Phys. D Appl. Phys.* **36**, 2152–2156.

Pagot, E., Cloetens, P., Fiedler, S., Bravin, A., Coan, P., Baruchel, J., Härtwig, J. & Thomlinson, W. (2003). *Appl. Phys. Lett.* **82**, 3421–3423.

Pfeiffer, F., Bech, M., Bunk, O., Kraft, P., Eikenberry, E. F., Brönnimann, C., Grünzweig, C. & David, C. (2008). *Nat. Mater.* **7**, 134–137.

Rigon, L., Arfelli, F. & Menk, R. H. (2007*a*). *Appl. Phys. Lett.* **90**, 114102.

Rigon, L., Arfelli, F. & Menk, R. H. (2007*b*). *J. Phys. D Appl. Phys.* **40**, 3077–3089.

Rigon, L., Besch, H. J., Arfelli, F., Menk, R. H., Heitner, G. & Plothow-Besch, H. (2003). *J. Phys. D Appl. Phys.* **36**, A107–A112.

Suhonen, H., Fernández, M., Bravin, A., Keyriläinen, J. & Suortti, P. (2007). *J. Synchrotron Rad.* **14**, 512–521.

Suortti, P., Keyriläinen, J. & Thomlinson, W. (2013). *J. Phys. D Appl. Phys.* **46**, 494002.
Wernick, M. N., Wirjadi, O., Chapman, D., Zhong, Z., Galatsanos, N. P., Yang, Y., Brankov, J. G., Oltulu, O., Anastasio, M. A. & Muehleman, C. (2003). *Phys. Med. Biol.* **48**, 3875–3895.
Yuan, Q., Zhang, K., Hong, Y., Huang, W., Gao, K., Wang, Z., Zhu, P., Gelb, J., Tkachuk, A., Hornberger, B., Feser, M., Yun, W. & Wu, Z. (2012). *J. Synchrotron Rad.* **19**, 1021–1028.
Yuan, Q., Zhu, P., Wang, J., Huang, W., Shu, H., Hu, T. & Wu, Z. (2006). *Radiat. Phys. Chem.* **75**, 1990–1994.